On the acoustic signature of tandem airfoils: The sound of an elastic airfoil in the wake of a vortex generator

A. Manela

Citation: Physics of Fluids **28**, 071905 (2016); doi: 10.1063/1.4958661
View online: http://dx.doi.org/10.1063/1.4958661
View Table of Contents: http://scitation.aip.org/content/aip/journal/pof2/28/7?ver=pdfcov
Published by the AIP Publishing

PHYSICS OF FLUIDS **28**, 071905 (2016)

On the acoustic signature of tandem airfoils: The sound of an elastic airfoil in the wake of a vortex generator

A. Manela
Faculty of Aerospace Engineering, Technion - Israel Institute of Technology, Haifa 32000, Israel

(Received 22 July 2015; accepted 29 June 2016; published online 20 July 2016)

The acoustic signature of an acoustically compact tandem airfoil setup in uniform high-Reynolds number flow is investigated. The upstream airfoil is considered rigid and is actuated at its leading edge with small-amplitude harmonic pitching motion. The downstream airfoil is taken passive and elastic, with its motion forced by the vortex-street excitation of the upstream airfoil. The non-linear near-field description is obtained via potential thin-airfoil theory. It is then applied as a source term into the Powell-Howe acoustic analogy to yield the far-field dipole radiation of the system. To assess the effect of downstream-airfoil elasticity, results are compared with counterpart calculations for a non-elastic setup, where the downstream airfoil is rigid and stationary. Depending on the separation distance between airfoils, airfoil-motion and airfoil-wake dynamics shift between in-phase (synchronized) and counter-phase behaviors. Consequently, downstream airfoil elasticity may act to amplify or suppress sound through the direct contribution of elastic-airfoil motion to the total signal. Resonance-type motion of the elastic airfoil is found when the upstream airfoil is actuated at the least stable eigenfrequency of the downstream structure. This, again, results in system sound amplification or suppression, depending on the separation distance between airfoils. With increasing actuation frequency, the acoustic signal becomes dominated by the direct contribution of the upstream airfoil motion, whereas the relative contribution of the elastic airfoil to the total signature turns negligible. *Published by AIP Publishing.* [http://dx.doi.org/10.1063/1.4958661]

I. INTRODUCTION

Airfoil aerodynamic sound has been a topic of extensive investigations over the years.[1] Nowadays, with the growing interest in reducing air-machinery noise, acoustic analyses of airfoil sound in various configurations appear frequently (e.g., Refs. 2–4). Apart from the fundamental interest in such investigations for civil- and military-flight applications, these works are relevant in a large number of bio-fluidic setups, ranging from biomedical studies on palatal snoring[5,6] to analyses on birds[7–10] and insect[11,12] flight sound, where wing noise has an important role as a form of social communication.[13,14]

Compared with single-airfoil studies, existing works on multi-body fluid-structure interaction problems have focused mainly on near-field investigations, with less emphasis on far-field radiation. Beginning with studies on the canonical double-cylinder configuration,[15] later investigations have focused, among others, on thin-structure setups (e.g., Refs. 16–18). The effect of body elasticity in a multi-body setup has also been incorporated in a number of works, dealing with critical and post-critical behaviors of groups of two and more flexible filaments immersed in uniform mean flow.[19–22] These works have been partially motivated by the propulsion efficiency gained by the motion of an elastic body in the wake of another,[23] as well as by energy-harvesting applications.[24]

While the acoustic radiation by multi-airfoil setups has received considerably less attention, such analyses appear to be of practical importance in a large number of natural and engineering applications. These cover a range of environments, including the acoustic radiation of formation-flight configurations and sound emission by multi-blade setups, common in engines and wind turbines. Within the context of formation-flight sound, it is of interest to examine how the sound

of a group combines the separate contributions of its members, and whether it is possible to identify specific configurations where the total radiation of a group suppresses its separate member signatures. In a sense, such a question may be considered parallel to near-field studies on the effect of formation setup on propulsion and energy harvesting efficiencies, only that it addresses a different aspect of the problem, the sound, and thus requires a different scheme of analysis.

Relatively few works have appeared on aerodynamic sound emission by multi-body setups. Among these studies, some investigations have been carried out on configurations containing airfoils. Thus, Casalino *et al.*[25] have predicted the noise produced by rod-airfoil interactions using the Ffowcs-Williams-Hawkings equations. Later on, Leclercq and Doolan[26] have investigated the sound generated by the interaction between a blade and a block, and Winkler and Carolus[27] and Gruber *et al.*[28] have suggested means for reducing tandem airfoil noise through active blowing and additional trailing and leading edge serrations, respectively.

Recently, the far-field radiation by a side-by-side airfoil configuration has been analyzed.[29] A setup of two identical rigid airfoils, actuated at their leading edges, has been considered. Imposing the dynamic description of airfoils motion, Ref. 29 has studied the acoustic field generated by the interaction between the actuated structures and the surrounding flow. Mechanisms of sound amplification and sound attenuation have been identified and rationalized based on the phase difference between airfoil actuations and wake-wake interactions. To model the system response to unsteady flow conditions, the far-field sound generation by the airfoils interaction with an incident line vortex has also been considered.

While the above set of works indicates on an increasing interest in acoustic analyses of multi-object systems, the general problems in hand still lack fundamental study. In particular, the effect of structure elasticity, prevalent in natural environments, has not been systematically investigated. The objective of the present work is to follow such an investigation by analyzing the acoustic signature of a tandem-airfoil setup with a downstream flexible structure. An upstream rigid airfoil acts as a "vortex generator," with its leading edge actuated in a periodic pitching motion. In marked difference from Ref. 29, the present work does not assume that the kinematics of the two bodies is imposed, but solves for the flow-induced motion of the elastic airfoil. This dynamic degree of freedom gives rise, as demonstrated below, to resonance-type motion of the downstream structure, which, in turn, can be used to suppress the overall radiation of the system.

We consider the above-described setup as a simple test-case which represents the dynamical state of a flexible structure in the wake of an upstream obstacle. Taking only one of the structures to be elastic and passive facilitates the examination of the separate effect of elasticity, as the results may be easily compared with a case where the body is replaced by a rigid and stationary airfoil. Apart from analyzing the effect of body elasticity on the acoustic radiation in a multi-body setup for the first time, the present investigation also extends on previous investigations of the sound of single (e.g., Ref. 30) and multiple[29] bodies subject to "incident" vorticity, by incorporating the cause of flow unsteadiness (here being the actuated upstream body), and its effect, into the scheme of solution. Notably, considering the chosen configuration as only one example, the scheme presented may be readily applied to investigate the radiation by various other setups, including non-tandem geometries with a larger number of airfoils.

The paper is organized as follows. In Sec. II, the hydrodynamic (near-field) and acoustic (far-field) problems are formulated. In Sec. III, details on problem scaling and numerical procedure of the solution are given. Our results are presented in Sec. IV. Remarkably, it is found that, depending on the separation distance between airfoils and the excitation frequency of the upstream body, elasticity may amplify or suppress sound, compared with a counterpart non-elastic system. Our conclusions are given in Sec. V.

II. FORMULATION OF THE PROBLEM

A. Near-field problem

A schematic description of the problem is shown in Figure 1. Consider a two-dimensional setting consisting of two infinitely thin airfoils of chord $2a$. The airfoils are nominally placed along the x_1-direction in a tandem setup, with a separation distance of $2s$ between their mid-chords (or

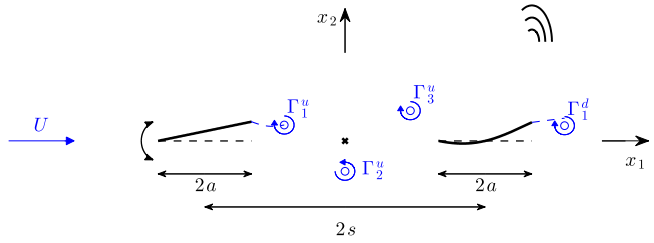

FIG. 1. Schematic of the tandem airfoil setup.

trailing- or leading-edges). The system is subject to low-Mach uniform flow of magnitude U in the x_1-direction. The upstream airfoil (hereafter denoted by superscript "u") is considered rigid, while the downstream airfoil (denoted by superscript "d") is elastic and inextensible. At time $t \geq 0$, harmonic pitching actuation of frequency ω and amplitude $\bar{\varepsilon}$ (with an overbar denoting a non-dimensional quantity) is applied at the leading edge of the upstream airfoil,

$$\left.\frac{\partial \xi^u}{\partial x_1}\right|_{x_1=-s-a} = \bar{\varepsilon}\sin(\omega t), \tag{1}$$

where $\xi^u(x_1,t)$ denotes the displacement of the upstream airfoil. It is assumed that the pitching amplitude $\bar{\varepsilon}$ is sufficiently small so that the problem may be linearized about its nominal state and thin-airfoil theory can be applied. The downstream airfoil is assumed "passive," with its motion induced by the pitching motion and vorticity release of the upstream wing. The small mean-flow Mach number assumed allows the near-field flow to be treated as incompressible and potential. Given the small angles of attack considered, leading edge flow detachments are excluded at the outset, and fluid vorticity is allowed only along the trailing edge wakes of the airfoils. A similar assumption has been made in previous studies on flows generated around thin elastic structures (e.g., Refs. 31 and 32), including cases where the interactions of a sequence of upstream line vortices with thin bodies have been considered.[19,33] Inclusion of the impact of leading edge separation, governed by viscous effects, is beyond the scope of the present contribution.

We formulate an initial value problem, where at $t = 0$ the airfoils are aligned with the x_1-axis, and upstream leading edge actuation is commenced. In accordance with the potential thin-airfoil theory, trailing edge singularity is induced by airfoil motion interactions with the surrounding fluid. This singularity is regularized by the application of the unsteady Kutta condition and results in the release of vorticity at the airfoils' trailing edges. The description of trailing-edge wakes in two-dimensional configurations may be carried out using either continuous- or discrete-type models. In the former, the wake is described via a thin vortex sheet, starting at the body downstream end, and representing continuous shedding of vorticity. In the latter, wake vorticity is discretized as a set of concentrated core vortices. While there appear different views regarding the applicability of each of the descriptions for capturing the wake dynamics in a given setup,[34,35] discrete models have been routinely used in a large number of configurations. In the present problem, the discrete approach is particularly preferred as it simplifies the description of non-linear interaction of the upstream wake with the downstream body. This is mainly since a continuous model cannot assume that the vortex sheet is placed along the x_1-axis, as it must be deviated by the downstream airfoil located along the same axis. Mathematically, this is expected to complicate the analysis considerably.

Adopting a discrete-type approach, we apply the Brown and Michael scheme to describe the wake evolution.[36,37] This is a prevalent method to model vortex shedding phenomena from two-dimensional sharp ends at high Reynolds number flows and has been applied in a large number of investigations on airfoil aerodynamic sound.[3,4,29,30,38–40] According to the scheme, the wake is described as a set of discrete line vortices whose positions and strengths vary with time. At a given time, one vortex is being shed from the body trailing edge, in the form of a thin connecting sheet of infinitesimal circulation ending in a concentrated core of finite circulation. The core strength changes with time according to Kelvin theorem, while its position is governed by the Brown and

Michael formula (see Eq. (10)). When the time derivative of vortex strength changes sign, the vortex is detached from the thin sheet and propagates as a "free" line vortex with fixed circulation. The shedding of the next vortex is then initiated. Over the years, corrections have been suggested to the original Brown and Michael formula, to account for a spurious dipole induced by the time dependence of circulation of the shed vortex.[41,42] Discussion on these corrections, and justification for the application of the original Brown and Michael formula in a thin-airfoil configuration, as done here, is made in Ref. 30.

Formulation of the problem consists of a set of equations to govern the motion of airfoils and associated wake vortices. While some of the details of formulation appearing here and in Sec. II B are similar to previous statements of the problem for a single elastic[30] and rigid side-by-side airfoils,[29] they are recapitulated here for better clarity and completeness. In line with the boundary forcing (1) and the rigidity of upstream airfoil, its displacement is given by

$$\xi^u(x_1,t) = (x_1 + s + a)\bar{\varepsilon}\sin(\omega t), \tag{2}$$

where $-s-a \le x_1 \le -s+a$ and $t \ge 0$. Assuming small-amplitude motion of the downstream elastic airfoil, its displacement $\xi^d(x_1,t)$ is governed by the linearized form of the dynamical Euler-Bernoulli equation,[30]

$$\rho_s \frac{\partial^2 \xi^d}{\partial t^2} + EI\frac{\partial^4 \xi^d}{\partial x_1^4} = \Delta p(x_1,t), \tag{3}$$

balancing structure inertia, bending stiffness, and fluid loading terms. In Eq. (3), $s-a \le x_1 \le s+a$, ρ_s is the airfoil mass per unit area, and EI denotes the structural bending stiffness. On the right-hand side, $\Delta p = p_- - p_+$ symbols fluid pressure jump between airfoil lower (p_-) and upper (p_+) surfaces. It is through the pressure-jump term that structure and fluid dynamical problems are coupled, as discussed below.

Applying thin-airfoil methodology, each of the upstream and downstream airfoils is represented by the distribution of circulation per unit length, $\gamma_a^u(x_1,t)$ and $\gamma_a^d(x_1,t)$, respectively. To specify these distributions, impermeability conditions are imposed. Adopting two-dimensional complex-plane notation (with $z = x_1 + \mathrm{i}x_2$ denoting a complex variable), the conditions are given by[29]

$$\frac{\partial \xi^u}{\partial t} + U\frac{\partial \xi^u}{\partial x_1} = \mathrm{Im}\left\{\frac{\mathrm{i}}{2\pi}\left[\fint_{-s-a}^{-s+a}\frac{\gamma_a^u(p,t)\mathrm{d}p}{x_1-p} + \int_{s-a}^{s+a}\frac{\gamma_a^d(p,t)\mathrm{d}p}{x_1-p} + \sum_{k=1}^{n^u}\frac{\Gamma_k^u}{x_1 - z_{\Gamma_k^u}} + \sum_{k=1}^{n^d}\frac{\Gamma_k^d}{x_1 - z_{\Gamma_k^d}}\right]\right\}, \tag{4}$$

for the upstream airfoil (with $-s-a \le x_1 \le -s+a$) and

$$\frac{\partial \xi^d}{\partial t} + U\frac{\partial \xi^d}{\partial x_1} = \mathrm{Im}\left\{\frac{\mathrm{i}}{2\pi}\left[\int_{-s-a}^{-s+a}\frac{\gamma_a^u(p,t)\mathrm{d}p}{x_1-p} + \fint_{s-a}^{s+a}\frac{\gamma_a^d(p,t)\mathrm{d}p}{x_1-p} + \sum_{k=1}^{n^u}\frac{\Gamma_k^u}{x_1 - z_{\Gamma_k^u}} + \sum_{k=1}^{n^d}\frac{\Gamma_k^d}{x_1 - z_{\Gamma_k^d}}\right]\right\}, \tag{5}$$

for the downstream airfoil (where $s-a \le x_1 \le s+a$). In Eqs. (4) and (5), $z_{\Gamma_k^u}$ and $z_{\Gamma_k^d}$ denote the instantaneous locations of the kth trailing edge vortices (with circulations Γ_k^u and Γ_k^d, respectively) released from the upstream and downstream airfoils, respectively. Barred integral signs mark Cauchy principal value integrals. Summations in Eqs. (4) and (5) are carried out over all n^u and n^d wake vortices contained in the upstream and downstream airfoil wakes, respectively. Having introduced the vortex-sheet representation of the downstream airfoil $\gamma_a^d(x_1,t)$, the pressure jump Δp appearing on the right-hand side of Eq. (3) is given by Bernoulli's equation,

$$\Delta p(x_1,t) = -\rho_0\left(\frac{\partial}{\partial t}\int_{s-a}^{x_1}\gamma_a^d(s,t)\mathrm{d}s + U\gamma_a^d(x_1,t)\right), \tag{6}$$

where ρ_0 denotes the mean fluid density.

Dynamics of the trailing edge wake is governed by a sequence of equations for the motion of the discrete trailing edge vortices. Specifically, the equations of motion for the upstream-released

$\Gamma^u_1,\ldots,\Gamma^u_{n^u-1}$ and downstream-released $\Gamma^d_1,\ldots,\Gamma^d_{n^d-1}$ "frozen" trailing edge vortices are

$$\frac{\mathrm{d}z_{\Gamma^u_k}}{\mathrm{d}t} = W^*_{\Gamma^u_k} \quad \text{and} \quad \frac{\mathrm{d}z_{\Gamma^d_k}}{\mathrm{d}t} = W^*_{\Gamma^d_k}, \tag{7}$$

respectively, where asterisks denote complex conjugates of a complex number, and

$$W_{\Gamma^u_k} = U - \frac{\mathrm{i}}{2\pi}\left(\int_{-s-a}^{-s+a}\frac{\gamma^u_a(x_1,t)\mathrm{d}x_1}{z_{\Gamma^u_k}-x_1} + \int_{s-a}^{s+a}\frac{\gamma^d_a(x_1,t)\mathrm{d}x_1}{z_{\Gamma^u_k}-x_1} + \sum_{\substack{m=1\\m\neq k}}^{n^u}\frac{\Gamma^u_m}{z_{\Gamma^u_k}-z_{\Gamma^u_m}} + \sum_{m=1}^{n^d}\frac{\Gamma^d_m}{z_{\Gamma^u_k}-z_{\Gamma^d_m}}\right) \tag{8}$$

and

$$W_{\Gamma^d_k} = U - \frac{\mathrm{i}}{2\pi}\left(\int_{-s-a}^{-s+a}\frac{\gamma^u_a(x_1,t)\mathrm{d}x_1}{z_{\Gamma^d_k}-x_1} + \int_{s-a}^{s+a}\frac{\gamma^d_a(x_1,t)\mathrm{d}x_1}{z_{\Gamma^d_k}-x_1} + \sum_{m=1}^{n^u}\frac{\Gamma^u_m}{z_{\Gamma^d_k}-z_{\Gamma^u_m}} + \sum_{\substack{m=1\\m\neq k}}^{n^d}\frac{\Gamma^d_m}{z_{\Gamma^d_k}-z_{\Gamma^d_m}}\right) \tag{9}$$

are the conjugate velocities induced at each of the instantaneous vortex locations, after removing their self-singularities. In line with the above discussion on the Brown and Michael theory, the time-varying strengths and positions of the instantaneously shed n^uth and n^dth trailing edge vortices are governed by the Brown and Michael equations

$$\frac{\mathrm{d}z_{\Gamma^u_{n^u}}}{\mathrm{d}t} + \left(z_{\Gamma^u_{n^u}} - z^u_{\mathrm{TE}}\right)\frac{1}{\Gamma^u_{n^u}}\frac{\mathrm{d}\Gamma^u_{n^u}}{\mathrm{d}t} = W^*_{\Gamma^u_{n^u}} \quad \text{and} \quad \frac{\mathrm{d}z_{\Gamma^d_{n^d}}}{\mathrm{d}t} + \left(z_{\Gamma^d_{n^d}} - z^d_{\mathrm{TE}}\right)\frac{1}{\Gamma^d_{n^d}}\frac{\mathrm{d}\Gamma^d_{n^d}}{\mathrm{d}t} = W^*_{\Gamma^d_{n^d}}, \tag{10}$$

where $W_{\Gamma^u_{n^u}}$ and $W_{\Gamma^d_{n^d}}$ are given by Eqs. (8) and (9) with $k = n^u$ and $k = n^d$, respectively, and z^u_{TE} and z^d_{TE} denote instantaneous complex-variable locations of airfoils trailing edges. The strength of shed vortices is specified by the Kelvin theorem

$$\Gamma^u_{n^u}(t) = -\int_{-s-a}^{-s+a}\gamma^u_a(x_1,t)\mathrm{d}x_1 - \sum_{k=1}^{n^u-1}\Gamma^u_k \quad \text{and} \quad \Gamma^d_{n^d}(t) = -\int_{s-a}^{s+a}\gamma^d_a(x_1,t)\mathrm{d}x_1 - \sum_{k=1}^{n^d-1}\Gamma^d_k, \tag{11}$$

ensuring that the total sum of circulations of each airfoil and its wake vanishes at all times.

Formulation of the near-field problem is completed by prescribing clamped-free boundary conditions at the downstream airfoil endpoints,

$$\xi^d(s-a,t) = \left(\frac{\partial\xi^d}{\partial x_1}\right)_{(s-a,t)} = 0 \quad \text{and} \quad \left(\frac{\partial^2\xi^d}{\partial x_1^2}\right)_{(s+a,t)} = \left(\frac{\partial^3\xi^d}{\partial x_1^3}\right)_{(s+a,t)} = 0, \tag{12}$$

and imposing the unsteady Kutta condition,

$$\gamma^u_a(-s+a,t) = \gamma^d_a(s+a,t) = 0, \tag{13}$$

to ensure that the flow velocity at each trailing edge is finite. We assume that the release of trailing edge vorticity at each airfoil commences at $t = 0$; the system evolution is then followed for $t > 0$ via numerical integration. Details regarding the problem scaling and numerical analysis are given in Sec. III.

B. Far-field radiation

Following the formulation of the near-field problem, the system far acoustic field is now analyzed. In line with the present low-Mach and high-Reynolds-number flow setup, we start with the homentropic form of the Powell-Howe vortex sound equation (Eq. (5.2.7) in Ref. 43),

$$\left(\frac{1}{c_0^2}\frac{\partial^2}{\partial t^2} - \boldsymbol{\nabla}^2\right)B = \mathrm{div}\left(\boldsymbol{\Omega}\times\mathbf{v}\right), \tag{14}$$

where c_0 is the mean speed of sound, $B(\mathbf{x},t) = \int \mathrm{d}p/\rho + v^2/2$ denotes the fluid total enthalpy for homentropic flow (with p, ρ, and v marking fluid acoustic pressure, density, and velocity magnitude,

respectively), and $\mathbf{v}$ and $\mathbf{\Omega}$ are the fluid velocity and vorticity vectors, respectively. The vorticity vector is composed of the discrete contributions of upstream and downstream wake vortices,

$$\mathbf{\Omega} = \mathbf{\Omega}_{\Gamma^u} + \mathbf{\Omega}_{\Gamma^d}, \tag{15}$$

where

$$\mathbf{\Omega}_{\Gamma^u} = \hat{\mathbf{x}}_\mathbf{3} \sum_{k=1}^{n^u} \Gamma_k^u \delta\left(\mathbf{x} - \mathbf{x}_{\mathbf{\Gamma_k^u}}(\mathbf{t})\right) \quad \text{and} \quad \mathbf{\Omega}_{\Gamma^d} = \hat{\mathbf{x}}_\mathbf{3} \sum_{k=1}^{n^d} \Gamma_k^d \delta\left(\mathbf{x} - \mathbf{x}_{\mathbf{\Gamma_k^d}}(\mathbf{t})\right), \tag{16}$$

and δ denotes the Dirac delta function. In the far-field ($|\mathbf{x}| \to \infty$),

$$B(\mathbf{x},t) \approx p(\mathbf{x},t)/\rho_0, \tag{17}$$

and we focus on expressing the distant $|\mathbf{x}| \to \infty$ approximation for $p(\mathbf{x},t)$.

The problem for $B(\mathbf{x},t)$ is analyzed using a Green's function approach. Towards this end, we introduce the counterpart problem for the Green's function $G(\mathbf{x},\mathbf{y},t-\tau)$,

$$\left(\frac{1}{c_0^2}\frac{\partial^2}{\partial t^2} - \nabla^2\right) G = \delta(\mathbf{x}-\mathbf{y})\,\delta(t-\tau), \tag{18}$$

where $\mathbf{x}$ and $\mathbf{y}$ denote the observer and point-source vector locations, respectively, and τ is the time instant of point-source action. Taking into account of the airfoil surfaces, and with no loss of generality, we impose a Neumann-type boundary condition of a vanishing normal derivative of G over the airfoils boundaries, $(\partial G/\partial y_n)_{\text{airfoils}} = 0$. Multiplying Eq. (14) by $G(\mathbf{x},\mathbf{y},t-\tau)$, subtracting Eq. (18) multiplied by $B(\mathbf{x},t)$, making use of the inviscid form of Crocco's equation,

$$\frac{\partial \mathbf{v}}{\partial t} + \mathbf{\Omega} \times \mathbf{v} = -\nabla B,$$

and integrating over the volume of fluid and time, we obtain the following expression for $B(\mathbf{x},t)$ in terms of the Green's function,

$$B(\mathbf{x},t) = -\int_{-\infty}^{\infty} \mathrm{d}\tau \int_{-\infty}^{\infty} (\mathbf{\Omega} \times \mathbf{v}) \nabla G \mathrm{d}^3\mathbf{y} + \int_{-\infty}^{\infty} \mathrm{d}\tau \oint_{\text{airfoils}} \left(B\frac{\partial G}{\partial y_n} + G\frac{\partial v_n}{\partial \tau}\right) \mathrm{d}S(\mathbf{y}), \tag{19}$$

where v_n denotes the component of fluid velocity normal to the airfoils. Applying the condition $(\partial G/\partial y_n)_{\text{airfoils}} = 0$ and making use of Eq. (17), we arrive at an expression for the far-field acoustic pressure,

$$p(\mathbf{x},t) \approx -\int_{-\infty}^{\infty} \mathrm{d}\tau \int_{-\infty}^{\infty} \rho_0 (\mathbf{\Omega} \times \mathbf{v}) \nabla G \mathrm{d}^3\mathbf{y} + \int_{-\infty}^{\infty} \mathrm{d}\tau \oint_{\mathcal{S}^u} \rho_0 G \frac{\partial v_n}{\partial \tau} \mathrm{d}S(\mathbf{y}) + \int_{-\infty}^{\infty} \mathrm{d}\tau \oint_{\mathcal{S}^d} \rho_0 G \frac{\partial v_n}{\partial \tau} \mathrm{d}S(\mathbf{y}), \tag{20}$$

where $\mathcal{S}^u$ and $\mathcal{S}^d$ denote the upstream and downstream airfoil surfaces, respectively. Making use of Eq. (20), the acoustic pressure can be written explicitly by the sum of "airfoils motion" and "wakes vorticity" contributions,

$$p(\mathbf{x},t) = p_\xi(\mathbf{x},t) + p_\Omega(\mathbf{x},t), \tag{21}$$

where

$$p_\xi(\mathbf{x},t) = p_\xi^u(\mathbf{x},t) + p_\xi^d(\mathbf{x},t) = \rho_0 \frac{\partial}{\partial t}\left[\int_0^\infty \left(\frac{\partial \xi^u}{\partial \tau}\oint_{\mathcal{S}^u} G(\mathbf{x},\mathbf{y},t-\tau)\mathrm{d}S(\mathbf{y}) + \frac{\partial \xi^d}{\partial \tau}\oint_{\mathcal{S}^d} G(\mathbf{x},\mathbf{y},t-\tau)\mathrm{d}S(\mathbf{y})\right)\mathrm{d}\tau\right] \tag{22}$$

and

$$p_\Omega(\mathbf{x},t) = p_\Omega^u(\mathbf{x},t) + p_\Omega^d(\mathbf{x},t) = -\rho_0 \int_0^\infty \left(\sum_{k=1}^{n^u} \int_{\mathcal{V}_{\Gamma_k^u}} (\mathbf{\Omega}_{\Gamma_k^u} \times \mathbf{V}_{\Gamma_k^u}) \cdot \frac{\partial G}{\partial \mathbf{y}}(\mathbf{x},\mathbf{y},t-\tau)\mathrm{d}\mathbf{y} + \sum_{k=1}^{n^d} \int_{\mathcal{V}_{\Gamma_k^d}} (\mathbf{\Omega}_{\Gamma_k^d} \times \mathbf{V}_{\Gamma_k^d}) \cdot \frac{\partial G}{\partial \mathbf{y}}(\mathbf{x},\mathbf{y},t-\tau)\mathrm{d}\mathbf{y}\right)\mathrm{d}\tau. \tag{23}$$

In (22) and (23), $\mathcal{V}_{\Gamma_k^u}$ and $\mathcal{V}_{\Gamma_k^d}$ denote fluid regions occupied by the upstream and downstream trailing edge vortices, $\mathbf{\Omega}_{\Gamma_k^u}$ and $\mathbf{\Omega}_{\Gamma_k^d}$ represent their vorticities, and $\mathbf{V}_{\Gamma_k^u}$ and $\mathbf{V}_{\Gamma_k^d}$ their instantaneous velocities.

We focus on a case where the tandem airfoil setup is acoustically compact, by assuming that the acoustic wavelength is large compared with the characteristic length-scale of the source zone. Taking the latter to be airfoils common half-chord a or half-distance separation s, and writing the acoustic wavelength as $2\pi c_0/\omega$, source compactness requires that sound frequency satisfies $\omega \ll 2\pi c_0/a$ and $\omega \ll 2\pi c_0/s$. Recalling that $s > a$ by virtue of the geometrical setup (see Fig. 1), the latter is more restricting. Source compactness is therefore ensured at separation distances satisfying $s \ll 2\pi c_0/\omega$. Setting $c_0 \approx 340$ m/s and $\omega = 2\pi f$ (with f denoting the excitation frequency in Hz), this condition becomes $s \ll 340/f$, where s is measured in meters. For an audible source excitation with $f = 50$ Hz, the condition on s becomes $s \ll 7$ m. Such a restriction appears feasible in the formation flight of birds, for which typical wingbeat frequencies are even lower, thus allowing for larger separation distances.[44] In a non-dimensional formulation, scaling the angular frequency by the convective unit U/a (as done in Sec. III), the condition becomes $\bar{\omega} \ll 2\pi a/Ms$ for $\bar{\omega} = \omega a/U$, where $M = U/c_0$ is the mean-flow Mach number. In addition to taking $M \ll 1$, it is therefore required that the airfoils are not too far apart and that $\bar{\omega} \lesssim O(1)$, so that $M\bar{\omega}s/a \ll 2\pi$. This assumes that the distance between the airfoils is much smaller than between the listener and each of the structures, so that far-field phase differences due to the size of the source zone become negligible.

In accordance with above assumptions on problem two-dimensionality and system compactness, the two-dimensional form of the compact Green's function is applied (Eq. (6.1.5) in Ref. 43)

$$G(\mathbf{x},\mathbf{y},t-\tau) \approx \frac{\mathbf{x}\cdot\mathbf{Y}}{2\pi\sqrt{2c_0|\mathbf{x}|^3}}\frac{\partial}{\partial t}\left\{\frac{\mathrm{H}(t_r-\tau)}{\sqrt{t_r-\tau}}\right\}, \quad |\mathbf{x}| \to \infty \tag{24}$$

to evaluate the acoustic far-field. Here, $\mathbf{x} = (x_1, x_2)$; H is a unit step function; and $t_r = t - |\mathbf{x}|/c_0$ is the *acoustic retarded time*. $\mathbf{Y}(\mathbf{y})$ denotes the *Kirchhoff* vector for the tandem-airfoil configuration, given by

$$\mathbf{Y}(\mathbf{y}) = (y_1, Y_2(y_1, y_2)), \tag{25}$$

where $Y_2(y_1, y_2)$ is the potential of uniform flow of unity magnitude in the y_2-direction over the double-airfoil system (see Eq. (3.4.8) *et seq.* in Ref. 43).

Following the derivation of Eq. (20) for the acoustic pressure, the Green's function and its associated flow potentials appearing in the Kirchhoff vector must satisfy the impermeability conditions on the stationary airfoil surfaces. Making use of Sedov's formula for the potential flow over a set of fixed coplanar airfoils,[45] we find for the complex conjugate representation of the velocity field

$$W(z) = \frac{\mathrm{i}\left[(s+a)^2\left(1+\mathrm{E}(\beta)/\mathrm{K}(\beta)\right)-z^2\right]}{\sqrt{\left[z^2-(s-a)^2\right]\left[z^2-(s+a)^2\right]}}. \tag{26}$$

The unit-flow potential $Y_2(y_1, y_2)$ (being the real part of the complex potential associated with $W(z)$) is obtained through numerical quadrature of Eq. (26). Appearing in (26) are

$$\mathrm{E}(\beta) = \int_0^{\pi/2}\left(1-\beta^2\sin^2\alpha\right)^{1/2}\mathrm{d}\alpha \quad \text{and} \quad \mathrm{K}(\beta) = \int_0^{\pi/2}\left(1-\beta^2\sin^2\alpha\right)^{-1/2}\mathrm{d}\alpha,$$

denoting complete elliptic integrals, where $\beta = 2\sqrt{sa}/(s+a)$ is fixed for a given tandem-setup geometry.

Substitution of $G(\mathbf{x},\mathbf{y},t-\tau)$ (Eq. (24)) into Eqs. (22) and (23) yields specific expressions for the upstream- and downstream-airfoil contributions to p_ξ and p_Ω. Starting with $p_\xi^u(\mathbf{x},t)$, substitute Eqs. (24) and (2) into the ξ^u-part in (22). The time integration can be carried out explicitly, to yield[29]

$$p_\xi^u(\mathbf{x},t) \approx -\frac{\bar{\varepsilon}\rho_0\omega^{5/2}\cos\theta}{4\sqrt{\pi c_0|\mathbf{x}|}}\left(\sin(\omega t_r)+\cos(\omega t_r)\right)\oint_{\mathcal{S}^u}(y_1+s+a)Y_2(y_1,y_2)\mathrm{d}S(\mathbf{y}). \tag{27}$$

A similar calculation, yet with ξ^d unknown (and obtained numerically through solution of the near-field problem in Sec. II A), yields

$$p_{\xi}^{d}(\mathbf{x},t) \approx \frac{\rho_0 \cos\theta}{2\pi\sqrt{2c_0|\mathbf{x}|}} \frac{\partial^2}{\partial t^2} \left[\int_0^{t_r} \frac{\mathrm{d}\tau}{\sqrt{t_r-\tau}} \oint_{S^d} \frac{\partial \xi^d(y_1,\tau)}{\partial \tau} Y_2(y_1,y_2)\mathrm{d}S(\mathbf{y}) \right]. \tag{28}$$

Eqs. (27) and (28) express the leading-order dipole contributions of direct airfoils motion to the far-field sound radiation, with the dipole axis oriented along the x_2-direction, and $\cos\theta = x_2/|\mathbf{x}|$ denoting observer directivity.

To evaluate the vortex sound component p_Ω, Eq. (24) is substituted into Eq. (23) together with Eq. (16), to yield explicit expressions for the separate contributions of upstream, p_Ω^u, and downstream, p_Ω^d, airfoil wake noise components. The general expressions are identical to those appearing in Eq. (23) in Ref. 29 and are not repeated here for brevity. In total, $p_\Omega = p_\Omega^u + p_\Omega^d$. We note that, apart from the "lift dipole" found for p_ξ, the wake dipole also contains a "suction" component oriented along the mean-flow direction x_1 (proportional to $\sin\theta$). This component originates from the non-linear wake-airfoils interaction, causing vortices motion in both mean-flow and normal directions.

III. SCALING AND NUMERICAL ANALYSIS

The near- and far-field problems formulated in Sec. II are now scaled to obtain a non-dimensional problem. Normalizing the length, velocity, time, and pressure by $a, U, a/U$, and $\rho_0 U^2$, respectively, we find that the non-dimensional equation of motion (3) for the elastic airfoil becomes

$$\frac{\partial^2 \bar{\xi}^d}{\partial \bar{t}^2} + \frac{1}{\bar{\alpha}^2} \frac{\partial^4 \bar{\xi}^d}{\partial \bar{x}_1^4} = \frac{1}{\bar{\mu}} \Delta \bar{p}, \tag{29}$$

where

$$\bar{\mu} = \frac{\rho_s}{\rho a} \quad \text{and} \quad \bar{\alpha} = U\sqrt{\frac{\rho_s a^2}{EI}} \tag{30}$$

denote the ratios of airfoil to fluid mass, and of mean-flow speed to airfoil bending speed (with the bending speed given by $U_b = \sqrt{EI/\rho_s a^2}$), respectively. The single-airfoil eigenvalue problem associated with Eq. (29) has been studied in Ref. 46 to delineate the critical conditions for the onset of spontaneous structure flutter. To ensure that our small-amplitude assumption is satisfied, we focus on a *subcritical* case, where the unperturbed ($\xi^d \equiv 0$) airfoil state is stable. Specifically, we fix $\bar{\mu} = 10$ and $\bar{\alpha} = 1$, corresponding to stable conditions according to Ref. 46. Our numerical calculations indicate that no qualitative differences are observed when choosing other subcritical $(\bar{\mu}, \bar{\alpha})$ combinations, and we therefore consider the present choice as representative.

Omitting presentation of the full non-dimensional problem for brevity, we note that the scaled dynamical problem is also governed by

$$\bar{\varepsilon},\ \bar{\omega} = \omega a/U,\ \text{and}\ \bar{s} = s/a, \tag{31}$$

specifying the normalized pitching amplitude and frequency, and separation distance between the airfoils, respectively. To illustrate our results, we fix $\bar{\varepsilon} = 0.01$ in accordance with the small-amplitude assumption set in Sec. II A. We thereby focus on the effects of $\bar{\omega}$ and $\bar{s}$ on the far-field radiation of the system.

Adopting the scaling introduced, the non-dimensional form of the acoustic pressure (21) becomes

$$\frac{p(\mathbf{x},t)}{\rho_0 U^2} = \sqrt{\frac{M}{8|\bar{\mathbf{x}}|}} \Pi_{\mathrm{tot}}(\bar{t}_r,\theta) = \sqrt{\frac{M}{8|\bar{\mathbf{x}}|}} \left(\Pi_\xi(\bar{t}_r,\theta) + \Pi_\Omega(\bar{t}_r,\theta) \right), \tag{32}$$

where

$$\Pi_{\bar{\xi}}(\bar{t}_r,\theta) = \Pi^u_{\bar{\xi}}(\bar{t}_r,\theta) + \Pi^d_{\bar{\xi}}(\bar{t}_r,\theta),$$
$$\Pi^u_{\bar{\xi}}(\bar{t}_r,\theta) \approx -\frac{\bar{\varepsilon}\bar{\omega}^{5/2}\cos\theta}{\sqrt{2\pi}}\left(\sin(\bar{\omega}\bar{t}_r)+\cos(\bar{\omega}\bar{t}_r)\right)\oint_{\bar{S}^u}(y_1+\bar{s}+1)\bar{Y}_2(\bar{y}_1,\bar{y}_2)\mathrm{d}S(\bar{\mathbf{y}}),$$
$$\Pi^d_{\bar{\xi}}(\bar{t}_r,\theta) \approx \frac{\cos\theta}{\pi}\frac{\partial^2}{\partial\bar{t}^2}\left[\int_0^{\bar{t}_r}\frac{\mathrm{d}\tau}{\sqrt{\bar{t}_r-\tau}}\oint_{\bar{S}^d}\frac{\partial\bar{\xi}^d(y_1,\tau)}{\partial\tau}\bar{Y}_2(\bar{y}_1,\bar{y}_2)\mathrm{d}S(\bar{\mathbf{y}})\right] \tag{33}$$

and

$$\Pi_{\Omega}(\bar{t}_r,\theta) = \Pi^u_{\Omega}(\bar{t}_r) + \Pi^d_{\Omega}(\bar{t}_r),$$
$$\Pi^u_{\Omega}(\bar{t}_r,\theta) \approx 2\sum_{k=1}^{n^u}\left[\sin\theta\frac{\partial}{\partial\bar{t}}\int_0^{\bar{t}_r}\frac{\bar{\Gamma}^u_k\bar{V}^{(2)}_{\Gamma^u_k}\mathrm{d}\tau}{\sqrt{\bar{t}_r-\tau}} - \cos\theta\frac{\partial}{\partial\bar{t}}\int_0^{\bar{t}_r}\bar{\Gamma}^u_k\left(\bar{V}^{(1)}_{\Gamma^u_k}\frac{\partial\bar{Y}_2}{\partial\bar{y}_2} - \bar{V}^{(2)}_{\Gamma^u_k}\frac{\partial\bar{Y}_2}{\partial\bar{y}_1}\right)_{\bar{\mathbf{x}}_{\Gamma^u_k}(\tau)}\frac{\mathrm{d}\tau}{\sqrt{\bar{t}_r-\tau}}\right],$$

$$\Pi^d_{\Omega}(\bar{t}_r,\theta)$$
$$\approx 2\sum_{k=1}^{n^d}\left[\sin\theta\frac{\partial}{\partial\bar{t}}\int_0^{\bar{t}_r}\frac{\bar{\Gamma}^d_k\bar{V}^{(2)}_{\Gamma^d_k}\mathrm{d}\tau}{\sqrt{\bar{t}_r-\tau}} - \cos\theta\frac{\partial}{\partial\bar{t}}\int_0^{\bar{t}_r}\bar{\Gamma}^d_k\left(\bar{V}^{(1)}_{\Gamma^d_k}\frac{\partial\bar{Y}_2}{\partial\bar{y}_2} - \bar{V}^{(2)}_{\Gamma^d_k}\frac{\partial\bar{Y}_2}{\partial\bar{y}_1}\right)_{\bar{\mathbf{x}}_{\Gamma^d_k}(\tau)}\frac{\mathrm{d}\tau}{\sqrt{\bar{t}_r-\tau}}\right]. \tag{34}$$

In (34), $\bar{\Gamma}^u_k = \Gamma^u_k/(2\pi aU)$, $\bar{\Gamma}^d_k = \Gamma^d_k/(2\pi aU)$, and $\bar{V}^{(j)}_{\Gamma^u_k}$ and $\bar{V}^{(j)}_{\Gamma^d_k}$ mark x_j-velocity components of the respective wake vortices. Results for the acoustic pressure are presented in terms of the acoustic "kernels" defined in (32)-(34). In addition to the parameters introduced in Eqs. (30) and (31), the non-dimensional acoustic pressure is governed by the observer direction, $\theta = \cos^{-1}(x_2/|\mathbf{x}|)$.

Numerical solution to the non-dimensional problem is obtained via discretization of the system of equations in both time (from $\bar{t}=0$ to some final time) and space (along airfoils chords). Space discretization is needed to express airfoils' vorticity distributions, $\bar{\gamma}^u_a(x_1,t)$ and $\bar{\gamma}^d_a(x_1,t)$, as well as for the numerical representation of the airfoil equation of motion (29). The numerical solution for the vorticity distributions is obtained via standard Fourier-expansion procedure, as described in Ref. 4 for a single airfoil. At each time step, the system of equations is discretized in space using a finite-difference scheme for the elastic-airfoil equation of motion. The equations are then integrated in time using a fourth-order Runge-Kutta algorithm. The typical time step used for integration was $\Delta\bar{t} = \pi/100\bar{\omega}$ (and fixed at $\Delta\bar{t} = \pi/100$ for $\bar{\omega} < 1$), which proved sufficient for the convergence of results.

IV. RESULTS

Having fixed the values of $\bar{\mu}, \bar{\alpha}$, and $\bar{\varepsilon}$ in Sec. III, we now turn to discuss the effects of separation distance $\bar{s} = s/a$ and pitching frequency $\bar{\omega}$ on system far-field radiation. To assess the impact of downstream airfoil elasticity (where the two airfoils combine into a "rigid-elastic" setup), we compare our results with those obtained for a counterpart "rigid-rigid" setup, where the downstream airfoil is rigid and stationary. Our numerical calculations invariably show that the lift dipole component ($\propto \cos\theta$, see (33) and (34)) is considerably larger than the suction dipole ($\propto \sin\theta$), and we therefore focus on the former in the following discussion. The effect of the suction dipole is included when introducing the measure of acoustic power (see Eq. (36)), presented in Figs. 4–7.

Figures 2-4 describe the hydrodynamic and acoustic fields generated by a tandem airfoil setup with separation distance $2\bar{s} = 6\pi$ and pitching frequency $\bar{\omega} = 1$. Starting with the near-field description, Fig. 2 shows time-variations of trailing edge displacements and airfoils total circulations (denoted by $\bar{\Gamma}_a = \Gamma_a/aU$) during the motion. For the latter, cases of rigid-rigid (Fig. 2(c)) and rigid-elastic (Fig. 2(d)) configurations are compared. Also presented in Fig. 2(b) is a time-snapshot of the vortical flow-field at quarter period ($\bar{t} = \bar{T}/4$, where $\bar{T} = 2\pi/\bar{\omega}$ is the pitching period), indicating instantaneous locations of the upstream-airfoil and downstream-airfoil wake vortices.

The results in Figs. 2(a), 2(c), and 2(d) indicate on an initial transient behavior of the system, starting at time $\bar{t}=0$ (when pitching motion commences), and evolving, at later times ($\bar{t} \gtrsim 35$), to

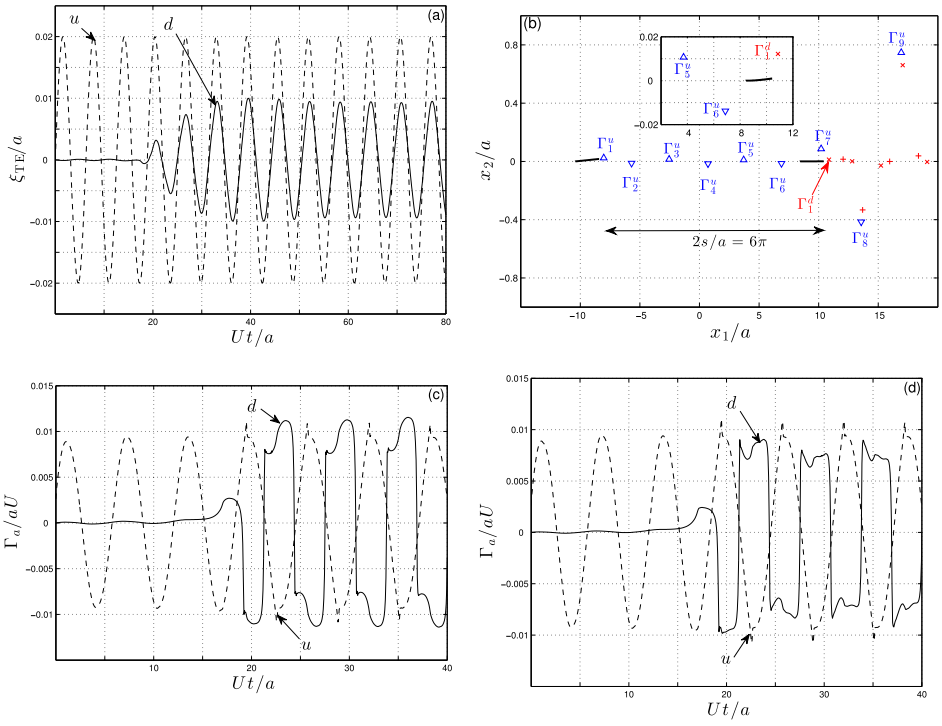

FIG. 2. The near-field of a tandem airfoil setup with $\bar{s} = 3\pi$ and $\bar{\omega} = 1$: (a) displacements of upstream (dashed) and downstream (solid) airfoil trailing edges in a rigid-elastic setup; (b) time snapshot of the vortical flow-field at quarter period ($\bar{t} = \bar{T}/4$) in a rigid-elastic setup, showing instantaneous locations of upstream- (blue) and downstream- (red) airfoil wake vortices (inset shows zoom into the vicinity of the downstream airfoil); (c) and (d) time variations of airfoil circulations in (c) rigid-rigid and (d) rigid-elastic configurations, with dashed and solid lines corresponding to upstream and downstream airfoils, respectively. In (b), △ and ▽ mark the wake vortices with positive and negative circulations, respectively, released from upstream airfoil; + and × denote the vortices with positive and negative circulations released from downstream airfoil.

periodic oscillations at the prescribed pitching frequency. The transient is illustrated by the initial vanishing and time-growing variations in the downstream airfoil displacement and circulation, reflecting the time it takes for the upstream-airfoil disturbance to affect the downstream structure. We hereby focus on the final periodic state obtained. Notably, the results indicate that, for the present combination of $\bar{s}$ and $\bar{\omega}$, oscillatory trailing edge displacements of the upstream (prescribed by Eq. (2)) and downstream (induced) airfoils occur in phase (synchronized), while airfoils circulations vary in counter-phase. The latter counter-phase behavior is viewed in both rigid-rigid and rigid-elastic configurations, as demonstrated by Figs. 2(c) and 2(d).

To rationalize the above finding, we make use of the vortical-field map shown in Fig. 2(b). Based on Kelvin's theorem, the sum of circulations of each airfoil and its associated wake must vanish at all times,

$$\bar{\Gamma}_a^u + \sum_{k=1}^{n^u} \bar{\Gamma}_k^u = 0, \quad \bar{\Gamma}_a^d + \sum_{k=1}^{n^d} \bar{\Gamma}_a^d = 0. \tag{35}$$

With all "frozen" wake vortices having fixed strengths, time-variations in total $\bar{\Gamma}_a^u$ and $\bar{\Gamma}_a^d$ circulations directly balance with instantaneous strengths of shed vortices $\bar{\Gamma}_{n^u}^u$ and $\bar{\Gamma}_{n^d}^d$ (denoted by $\bar{\Gamma}_1^u$ and $\bar{\Gamma}_1^d$ in Fig. 2(b)), respectively. The oscillatory motion of the upstream airfoil results in a vortex street with vortices of equal strengths and opposite signs (see the △ and ▽ symbols in Fig. 2(b) between $-\bar{s} + 1 < \bar{x}_1 < \bar{s} - 1$). During each pitching period ($\bar{T} = 2\pi/\bar{\omega}$), two vortices are detached from the upstream airfoil, at times $\bar{t} \approx \bar{T}/4$ and $\bar{t} \approx 3\bar{T}/4$ (when pitching angle is maximal). Estimating the streamwise velocity of a wake vortex to be unity (in mean-flow U units[47]), the travel time of a vortex

from initiation till reaching at the downstream airfoil trailing edge is $\Delta\bar{t} \approx 2\bar{s}$. During this time, $4\bar{s}/\bar{T}$ vortices are released, apart from the convected vortex.

The above kinematic description is supported by the vortical map presented in Fig. 2(b), where for $\bar{T} = 2\pi$ and $\bar{s} = 3\pi$, $n = 4\bar{s}/\bar{T} + 1 = 7$ upstream-wake vortices are found between $-\bar{s} + 1 < \bar{x}_1 < \bar{s} - 1$. The upstream vortices interact with the downstream airfoil as approaching it, with their trajectories affected by this non-linear interaction in accordance with their equation of motion and structure impermeability condition. At the time instant $\bar{t} = \bar{T}/4$ presented, the $\bar{\Gamma}_7^u$ vortex passes in the vicinity of the downstream airfoil trailing edge and induces the shedding of $\bar{\Gamma}_1^d$. In line with previous studies on the interaction of a single vortex with a thin airfoil (e.g., Ref. 38), the $\bar{\Gamma}_1^d$ vortex is obtained equal in strength and opposite in direction to $\bar{\Gamma}_7^u$ and follows, at later times, a "silent" vortex pair motion together with $\bar{\Gamma}_7^u$ (similar to the pairs containing $\bar{\Gamma}_8^u$ and $\bar{\Gamma}_9^u$ in Fig. 2(b)).

The in-phase and counter-phase behaviors of airfoil displacements and circulations can now be explained. For the chosen combination of $\bar{s} = 3\pi$ and $\bar{\omega} = 1$, system kinetics forces, at any given time, shedding of a downstream-airfoil vortex (Γ_1^d in Fig. 2(b)) that is approximately opposite in sign and equal in strength to the vortex being shed from the upstream airfoil (Γ_1^u in Fig. 2(b)). This, in accordance with Eq. (35), results in a counter-phase relation between airfoil circulations. The in-phase flapping motion of upstream and downstream airfoils is directly related, as it essentially reflects the motion induced by $\bar{\Gamma}_7^u$ (equal in both sign and direction to $\bar{\Gamma}_1^u$) on the trailing edge of the downstream airfoil. As discussed below, this kinematic description has an important effect on the system acoustic signature.

The acoustic far-field behavior of the $\bar{\omega} = 1$ and $\bar{s} = 3\pi$ system is presented in Figs. 3 and 4. Fig. 3 shows the separate contributions of the upstream and downstream airfoils to the direct-motion, wake, and total lift-dipole pressures, and Fig. 4 presents the overall acoustic signature of the system. As we concentrate on the periodic system behavior, the results from Fig. 3 onward are presented over a period time interval and correspond to the "late-time" periodic response. A comparison between rigid-elastic and rigid-rigid configurations is discussed.

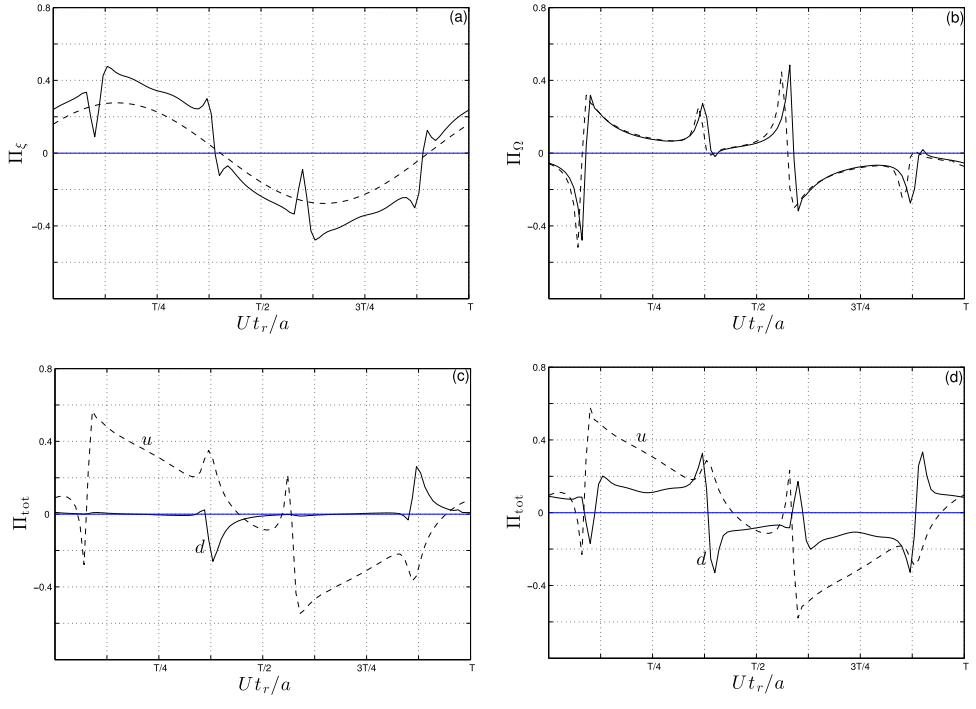

FIG. 3. Lift (at $\theta = 0$) dipole far-field for a tandem airfoil setup with $\bar{s} = 3\pi$ and $\bar{\omega} = 1$: (a) and (b) separate contributions of (a) direct airfoil noise, Π_ξ, and (b) wake noise, Π_Ω, for rigid-rigid (dashed) and rigid-elastic (solid) setups; (c) and (d) separate contributions of upstream (dashed) and downstream (solid) airfoils to the total acoustic signature in (c) rigid-rigid and (d) rigid-elastic setups. Thin blue lines show lines of zero pressures.

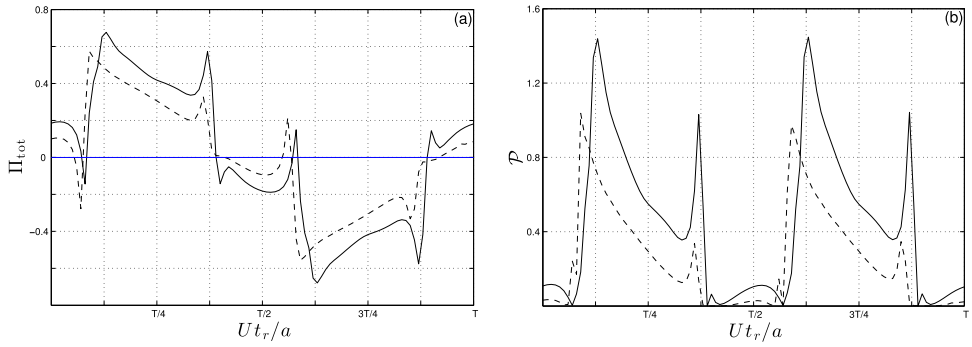

FIG. 4. Total far-field signature of rigid-rigid (dashed) and rigid-elastic (solid) tandem airfoil setups with $\bar{s} = 3\pi$ and $\bar{\omega} = 1$: (a) acoustic pressure in the normal (x_2-) direction; (b) system acoustic power. In (a), the thin blue line shows line of zero pressure.

Starting with the separate contributions in Fig. 3(a), we observe characteristic differences between the direct-motion signal Π_ξ of the rigid-rigid and rigid-elastic setups. In the rigid-rigid configuration, direct motion noise is generated by the upstream airfoil only (see Eq. (2)), leading to the sinusoidal pressure wave shown by the dashed line. The differences between the dashed and solid lines therefore reflect the effect of the downstream airfoil motion on the total direct-motion noise. In line with the synchronized motion of the two airfoils observed in Fig. 2(a), the added motion of the elastic airfoil leads to an increase in the value of Π_ξ over its counterpart rigid-rigid pressure. Notably, no similar effect is found in the wake Π_Ω component presented in Fig. 3(b): here, both configurations have nearly identical signatures (with a slight time-shift), indicating that airfoil elasticity has only a minor impact on the resulting wake sound. Comparing the separate contributions of upstream and downstream airfoils to the total sound in Figs. 3(c) and 3(d), it is also observed that the upstream-airfoil signature is nearly unaffected by downstream-airfoil elasticity (cf. the dashed lines between the figures). It is therefore concluded that differences between rigid-rigid and rigid-elastic airfoil configurations are mainly due, in this case, to the direct sound emitted by the elastic airfoil motion.

The total signatures of the $\bar{s} = 3\pi$ and $\bar{\omega} = 1$ systems are presented in Figure 4. To this end, the figure describes both the far field of the total lift ($\theta = 0$) dipole and the system non-dimensional *acoustic power*, defined by

$$\mathcal{P}(\bar{t}_r) = \int_0^{2\pi} \Pi_{\text{tot}}^2(\bar{t}_r, \theta)\, \mathrm{d}\theta, \tag{36}$$

and measuring the total instantaneous power (per unit length) radiated by the source. The results confirm that the downstream-airfoil elasticity leads to an increased noise level in the present case, where in-phase motion of the elastic airfoil is induced. In terms of sound pressure level, the difference between the curves in Fig. 4(a) amounts to a ≈3 dB increase in amplitude in the case of a rigid-elastic setup. The repeated form of the acoustic power in Fig. 4(b) between $0 \le \bar{t}_r \le \bar{T}/2$ and $\bar{T}/2 \le \bar{t}_r \le \bar{T}$ reflects the symmetry existing in the system dynamics along a period, visible also in Figs. 3 and 4(a), where the acoustic pressure is antisymmetric about $\bar{t}_r = \bar{T}/2$.

A. Effect of airfoils separation

To assess the effect of airfoil separation distance on system acoustic signature, we introduce the *average acoustic power*,

$$\mathcal{P}^* = \frac{1}{\bar{T}} \int_0^{\bar{T}} \mathcal{P}(\bar{t}_r) \mathrm{d}\bar{t}_r, \tag{37}$$

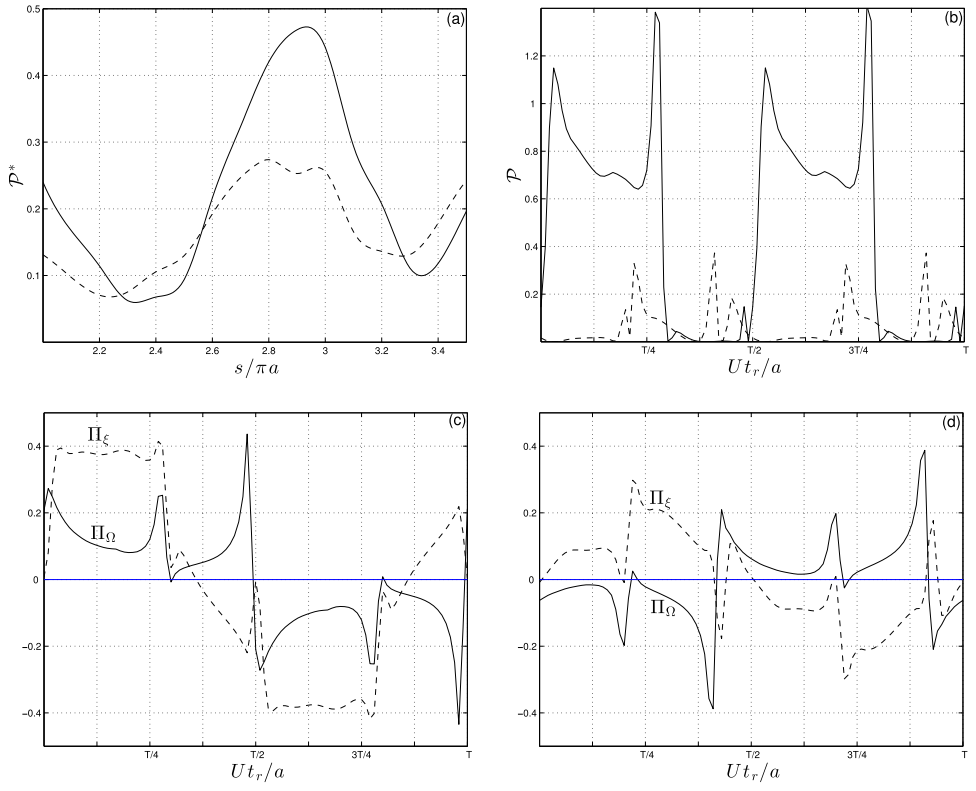

FIG. 5. Effect of airfoils separation distance $\bar{s}$ on system acoustic radiation at $\bar{\omega} = 1$: (a) variation of integrated acoustic power $\mathcal{P}^*$ with $\bar{s}/\pi$ for rigid-elastic (solid line) and rigid-rigid (dashed curve) setups; (b) system acoustic power for rigid-elastic setup with $\bar{s} = 2.9\pi$ (solid line) and $\bar{s} = 2.3\pi$ (dashed line); (c) and (d) separate contributions of direct airfoil motion noise, Π_ξ (dashed lines), and wake noise, Π_Ω (solid lines), in the $\theta = 0$ direction for rigid-elastic configuration with (c) $\bar{s} = 2.9\pi$ and (d) $\bar{s} = 2.3\pi$. In (c) and (d), thin blue lines show lines of zero pressures.

which can be considered as a measure for the overall noise emitted by the system in time. Based on Fig. 4(b), it is clear that $\mathcal{P}^*$ is larger in the rigid-elastic setup compared with the rigid-rigid case for $\bar{\omega} = 1$ and $\bar{s} = 3\pi$.

The variation of $\mathcal{P}^*$ with $\bar{s}/\pi$ for the case $\bar{\omega} = 1$ is presented in Figure 5(a), for both rigid-elastic (solid line) and rigid-rigid (dashed curve) airfoil setups. The two curves appear qualitatively similar, having nearly common maxima at $\bar{s} \approx 2.8\pi$ and $\bar{s} \approx 2.9\pi$, and local minima at $\bar{s} \approx 2.3\pi$ and $\bar{s} \approx 3.3\pi$. In line with our discussion in Figs. 3 and 4, these maxima and minima correspond to setups where downstream-airfoil radiation is in-phase or counter-phase to the sound emission by the upstream-airfoil, respectively. It is therefore concluded that, at the given mean-flow and pitching-frequency conditions, the separation distance may be used as a means for controlling the total system radiation. Notably, close to the local minima points, the mechanism of sound reduction by counter-phase interaction is found more efficient in the rigid-elastic case compared with the rigid-rigid setup. This is because, for these values of $\bar{s}$, the added effect of elastic-airfoil sound Π_ξ^d, missing in the rigid-rigid case, acts to further reduce the acoustic signal, as the downstream-airfoil motion occurs in phase opposition to the upstream-airfoil displacement. The situation is opposite close to the maximum point, where the downstream airfoil is displaced with the same phase as the upstream generator, and elasticity increases the total pressure amplitude (see Figs. 2(a) and 3(a)). The sound pressure levels associated with the results in Fig. 5(a) similarly indicate on a much stronger effect of airfoils separation distance on the noise in the rigid-elastic setup compared with the rigid-rigid system. Specifically, the variation with $\bar{s}$ between the maximal (in-phase) and minimal (counter-phase) values of $\mathcal{P}^*$ corresponds to a reduction of ≈8 dB in the sound pressure level of the rigid-elastic system, while only a ≈4 dB difference is obtained in the rigid-rigid setup.

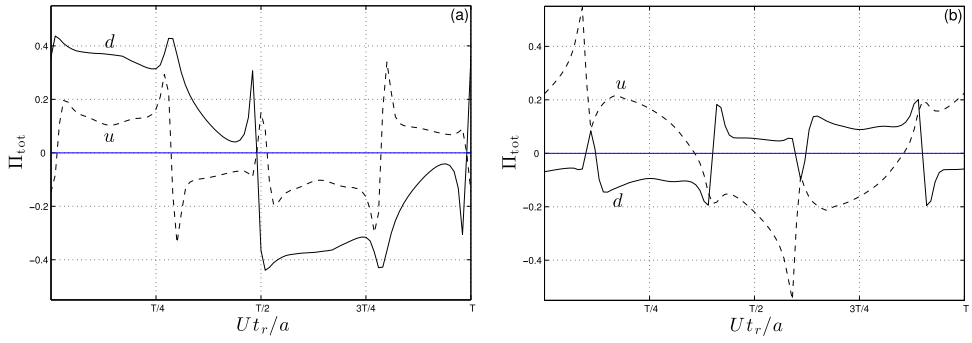

FIG. 6. Separate contributions of upstream (dashed) and downstream (solid) airfoils to the total far-field lift (at $\theta = 0$) dipole of a tandem airfoil setup with $\bar{\omega} = 1$ and (a) $\bar{s} = 2.9\pi$; (b) $\bar{s} = 2.3\pi$. Thin blue lines show lines of zero pressures.

Consequently, the pressure level associated with the minimum point of $\mathcal{P}^*$ at $\bar{s} \approx 2.3\pi$ is lower in $\approx$3 dB in the rigid-elastic system compared with the rigid-rigid configuration.

To further analyze the differences between the system behavior at in-phase and counter-phase conditions, Figs. 5(b)-5(d) present the acoustic signals obtained for a rigid-elastic setup at $\bar{s} = 2.9\pi$ and $\bar{s} = 2.3\pi$. Fig. 5(b) shows comparison between the system acoustic power in the two cases, indicating the comparable sound reduction found in the counter-phase ($\bar{s} = 2.3\pi$, dashed line) configuration. In-phase and counter-phase correlations between airfoils-motion and wake noise components are presented in Figs. 5(c) and 5(d), respectively, where it is seen that Π_ξ may act to either increase or decrease the total signature, depending on the value of $\bar{s}$. The in-phase and counter-phase interactions between the airfoils are further illustrated in Figure 6, which presents the separate contributions of upstream (dashed lines) and downstream (solid curves) airfoils to the total lift dipole for $\bar{s} = 2.9\pi$ (Fig. 6(a)) and $\bar{s} = 2.3\pi$ (Fig. 6(b)).

B. Effect of pitching frequency

Having analyzed the combined effects of separation distance $\bar{s}$ and airfoil elasticity on system acoustic radiation, we now focus on the impact of pitching frequency $\bar{\omega}$ on the results. To separate the effect of $\bar{\omega}$ from the effect of $\bar{s}$ on the system signature, variation in the pitching frequency should be accompanied by a change in the separation distance such that the product $\bar{s}\bar{\omega}$ is kept constant. This ensures that, with varying $\bar{\omega}$, the phase-difference properties of the system remain unchanged. Following the results in Figs. 2-4, we consider the case $\bar{s}\bar{\omega} = 3\pi$ and examine a rigid-elastic airfoil setup.

Figure 7(a) presents the variation with frequency of the amplitude of the elastic trailing-edge displacement. While the amplitude is bounded and small in all cases (in line with outset assumption on small airfoil displacements), a distinct maximum is observed at $\bar{\omega} \approx 0.85$. This maximum reflects on the eigenspectrum of the elastic airfoil and agrees well with the least stable eigenfrequency found previously at the same $(\bar{\mu}, \bar{\alpha})$ combination for the case of a single airfoil.[30] Physically, fluid-loading excitation of the elastic airfoil at its least stable eigenfrequency results in its largest induced oscillations. This is equivalent to an airfoil "choosing" to amplify its least stable eigenmode, as a result of a single line vortex passing in its vicinity, as found in Ref. 30.

The effect of the above "resonance-type" behavior on the system acoustic field is presented in Figs. 7(b) and 7(c), showing the acoustic power of the setup at $\bar{\omega} = 0.85$ (Fig. 7(b)) and $\bar{\omega} = 3$ (Fig. 7(c)), respectively, and comparing between rigid-rigid (dashed lines) and rigid-elastic (solid curves) configurations. Comparing between Figs. 7(b) and 7(c), we observe that the acoustic power in the $\bar{\omega} = 3$ case is one order of magnitude larger than in the $\bar{\omega} = 0.85$ setup. Moreover, the relative differences between rigid-rigid and rigid-elastic configurations are smaller in the $\bar{\omega} = 3$ case.

In line with the $\bar{s} = 3\pi/\bar{\omega}$ choice of parameter, the upstream and downstream airfoils are set in an "in-phase" configuration, where the sound of the rigid-elastic system is amplified compared with the rigid-rigid setup (cf. Fig. 4(b)). Our numerical calculations indicate that, with increasing

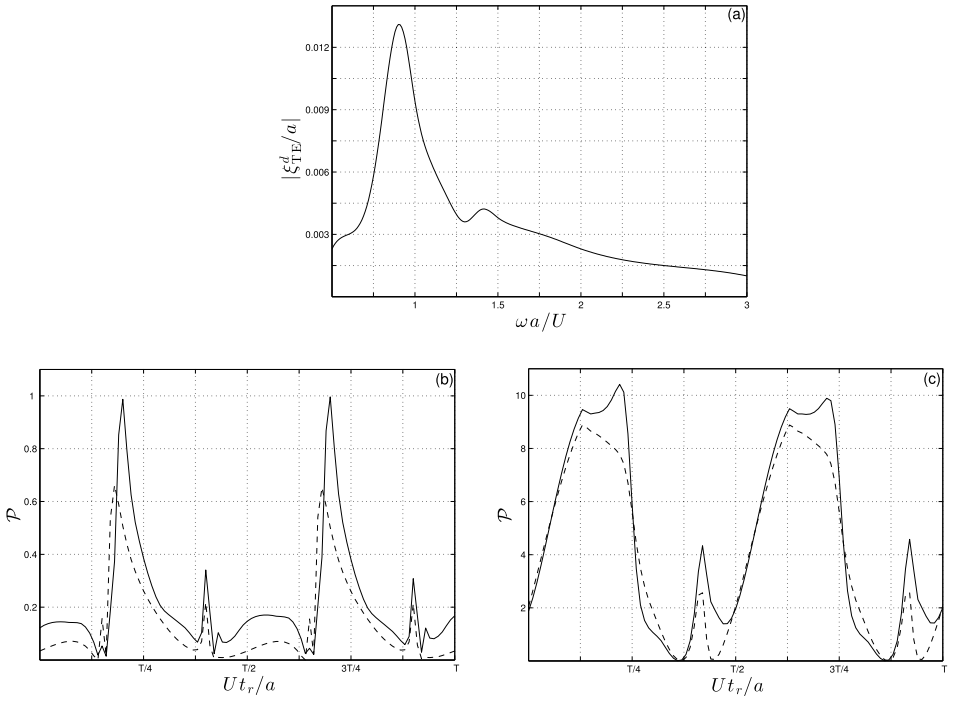

FIG. 7. Effect of pitching frequency $\bar{\omega}$ on the system acoustic radiation at $\bar{s} = 3\pi/\bar{\omega}$: (a) variation with frequency of maximum trailing-edge displacement for an elastic airfoil in a rigid-elastic setup; (b) and (c) acoustic power of rigid-rigid (dashed) and rigid-elastic (solid) systems at (b) $\bar{\omega} = 0.85$ and (c) $\bar{\omega} = 3$.

$\bar{\omega}$, the system acoustic signature becomes more and more dominated by the direct upstream-airfoil motion contribution[48] Π^u_ξ. Subsequently, the total radiation of the system increases with increasing $\bar{\omega}$, and the relative differences between rigid-rigid and rigid-elastic setups diminish. The effect of downstream-airfoil elasticity is mainly visible in the vicinity of the resonance frequency, where in-phase flapping of the downstream structure causes considerable increase in the total system radiation for the present choice of $\bar{s} = 3\pi/\bar{\omega}$. Inversely, when considering $\bar{s}\bar{\omega}$ values that correspond to counter-phase flapping (not presented here for brevity), the resonant motion of the downstream airfoil efficiently reduces the total sound level of the system below the counterpart rigid-rigid value. In this respect, the resonance-type motion may be considered beneficial.

V. CONCLUSION

We studied the acoustic signature of a tandem airfoil setup in uniform high-Reynolds and low-Mach number flow. The setup consisted of an upstream rigid airfoil and a downstream elastic airfoil, where the upstream airfoil was actuated at its leading edge with small-amplitude pitching motion, and the motion of the downstream structure was passively driven by the fluid. The hydrodynamic near-field description was obtained using potential thin-airfoil theory and was then applied to calculate the far-field sound through the Powell-Howe acoustic analogy. The specific effect of downstream-airfoil elasticity was assessed through comparison with results for a non-elastic setup, where the downstream airfoil was rigid and stationary. Depending on the separation distance between airfoils, it was shown that the motion of the airfoils and their wakes may shift between in-phase and counter-phase behaviors. Consequently, downstream-airfoil elasticity may act to amplify or suppress sound through the direct contribution of elastic-airfoil motion to the total radiation. Resonance-type motion of the elastic airfoil was found when the upstream airfoil was actuated at the least stable eigenfrequency of the downstream structure. This, again, resulted in overall sound amplification or suppression, depending on the separation distance between airfoils. With increasing actuation frequency, it was found that the acoustic signal becomes dominated by the

direct contribution of upstream airfoil motion, whereas the relative contribution of the elastic airfoil to the total signature turns negligible.

In view of previous *near-field* investigations of the fluid-structure interaction problem in similar setups,[16–20] a discussion on the differences between the near- and far-field investigations is in place. Primarily, near-field analyses assume incompressible flow conditions. This is different from the present acoustic investigation, where compressibility is taken into account within the framework of the acoustic analogy used (see Sec. II B). In addition, the results for the acoustic signature are qualitatively different from what has been observed in near-field investigations. In near-field studies, workers have sought for optimal flow conditions to maximize the energetic benefit (in terms of energy harvesting or improved propulsion efficiency) gained by the interaction between a passive structure and its vicinity. Yet, in the present work, the *total* acoustic signature of the tandem setup has been studied. With the objective to minimize the total far radiation of the system, we have looked for conditions where the sound produced by each of the airfoils tends to cancel the sound of the other. Generally, the total radiation much depends on the combined interaction between the two bodies and associated flow fields.

In contrast with previous works on the generation of sound by the interaction of single (e.g., Refs. 4, 30, and 38) and multiple[29] airfoils with incoming ("incident") flow vorticity, the present analysis fully models, to an extent that the potential-flow theory holds, the cause for incoming flow unsteadiness. This is carried out through the upstream-flow "vortex generator" (which, in turn, affects the specific form of Green's function used for the far-field analysis), which generates flow vorticity in accordance with its prescribed motion. The work has focused on a case where the upstream rigid body follows sinusoidal pitching excitation. Even so, the resulting far-field pressure was not monochromatic (even if periodic), and contained a range of higher-order harmonics, as reflected by the form of the pressure signal (see Figs. 4-7). A study on other forms (periodic or non-periodic) of the two-body excitation may be readily carried out using the present scheme.

Unlike Ref. 29, which considers the acoustic field of a side-by-side *rigid* airfoil setup, the present contribution investigates the effect of structure elasticity on the far-field radiation. This is done by solving for the motion of the elastic airfoil and coupling its dynamics into the computational scheme. The aeroelastic degree of freedom gives rise, as discussed above, to flow-induced motion of the downstream structure, which, in turn, can be used to considerably suppress or amplify the total acoustic field of the system. These effects are demonstrated through comparison with a counterpart non-elastic setup, where the downstream flexible airfoil is replaced by a rigid stationary structure. The comparison enables delineation and rationalization of the parameters range where elasticity acts to amplify or reduce sound (see, e.g., Fig. 5(a)). Thus, by taking into account the non-linearity of the near-field description, together with the coupling between the fluid and the aeroelastic properties of the material, the present contribution suggests a first systematic study on the impact of material flexibility on sound generation in a multi-airfoil configuration.

While the near-field problem considered was non-linear, it has been assumed, for application of thin-airfoil theory, that $\bar{\varepsilon}$, the amplitude of pitching excitation, is small. Additionally, we have focused on subcritical conditions for the motion of the elastic airfoil, to ensure that the angle of attack at the downstream airfoil is small enough. Evaluation of an $O(\bar{\varepsilon}^2)$ correction to our results requires formulation and solution to a higher-order problem, which is generally not in the scope of thin airfoil theory. The present analysis may be considered complementary to existing works on near-field dynamics of multiple filaments, where spontaneous (unforced) motion of the structures has been studied at supercritical conditions (e.g., Refs. 19, 20, and 22). Extension of the present acoustic analysis to include large-amplitude motions is a topic for future study, which would require a considerably more involved computational scheme.

[1] M. J. T. Smith, *Aircraft Noise* (Cambridge University Press, Cambridge, 1989).
[2] R. K. Amiet, "Airfoil gust response and the sound produced by airfoil-vortex interaction," J. Sound Vib. **107**, 487–506 (1989).
[3] Y. P. Guo, "Application of the Ffowcs Williams/Hawkings equation to two-dimensional problems," J. Fluid Mech. **403**, 201–221 (2000).
[4] A. Manela and L. Huang, "Point vortex model for prediction of sound generated by a wing with flap interacting with a passing vortex," J. Acoust. Soc. Am. **133**, 1934–1944 (2013).
[5] L. Huang, "Flutter of cantilevered plates in axial flow," J. Fluids Struct. **9**, 127–147 (1995).

[6] L. Huang, "Mechanical modeling of palatal snoring," J. Acoust. Soc. Am. **97**, 3642–3648 (1995).
[7] R. R. Graham, "The silent flight of owls," J. R. Aeronaut. Soc. **286**, 837–843 (1934).
[8] E. Sarradj, C. Fritzsche, and T. Geyer, "Silent owl flight: Bird flyover noise measurements," AIAA J. **49**, 769–779 (2011).
[9] K. Chen, Q. Liu, G. Liao, Y. Yang, L. Ren, H. Yang, and X. Chen, "The sound suppression characteristics of wing feather of owl (Bubo bubo)," J. Bionic Eng. **9**, 192–199 (2012).
[10] J. W. Jaworski and N. Peake, "Aerodynamic noise from a poroelastic edge with implications for the silent flight of owls," J. Fluid Mech. **723**, 456–479 (2013).
[11] H. C. Bennet-Clark, "Acoustics of insect song," Nature **234**, 255–259 (1971).
[12] J. Sueur, E. J. Tuck, and D. Robert, "Sound radiation around a flying fly," J. Acoust. Soc. Am. **118**, 530–538 (2005).
[13] S. Drosopoulos and M. F. E. Claridge, *Insect Sounds and Communication: Physiology, Behaviour, Ecology and Evolution* (Taylor and Francis, Boca Raton, FL, 2006).
[14] L. J. Cator, B. J. Arthur, L. C. Harrington, and R. R. Hoy, "Harmonic convergence in the love songs of the dengue vector mosquito," Science **323**, 1077–1079 (2009).
[15] M. M. Zdravkovich, "Review of flow interference between two circular cylinders in various arrangements," J. Fluids Eng. **99**, 618–633 (1977).
[16] H. Aziz and R. Mukherjee, "Unsteady aerodynamics of multiple airfoils in configuration," Int. J. Adv. Comput. Sci. **2**, 399–411 (2012).
[17] S. F. Harding and I. G. Bryden, "Generating controllable velocity fluctuations using twin oscillating hydrofoils," J. Fluid Mech. **713**, 150–158 (2012).
[18] Y. Bao and J. J. Tao, "Dynamic reactions of a free-pitching foil to the reverse kármán vortices," Phys. Fluids **26**, 031704 (2014).
[19] S. Alben, "Wake-mediated synchronization and drafting in coupled flags," J. Fluid Mech. **641**, 489–496 (2009).
[20] S. Kim, W. X. Huang, and H. J. Sung, "Constructive and destructive interaction modes between two tandem flexible flags in viscous flow," J. Fluid Mech. **661**, 511–521 (2010).
[21] F. B. Tian, H. Luo, L. Zhu, J. C. Liao, and X. Y. Lu, "An efficient immersed boundary-lattice boltzmann method for the hydrodynamic interaction of elastic filaments," J. Comput. Phys. **230**, 7266–7283 (2011).
[22] E. Uddin, W. X. Huang, and H. J. Sung, "Interaction modes of multiple flexible flags in a uniform flow," J. Fluid Mech. **729**, 563–583 (2013).
[23] J. C. Liao, D. Beal, G. V. Lauder, and M. S. Triantafyllou, "Fish exploiting vortices decrease muscle activity," Science **302**, 1566–1569 (2003).
[24] J. J. Allen and A. J. Smits, "Energy harvesting eel," J. Fluids Struct. **15**, 629–640 (2001).
[25] D. Casalino, M. Jacob, and M. Roger, "Prediction of rod-airfoil interaction noise using the Ffowcs-Williams-Hawkings analogy," AIAA J. **41**, 182–191 (2003).
[26] D. J. J. Leclercq and C. J. Doolan, "The interaction of a bluff body with a vortex wake," J. Fluids Struct. **25**, 867–888 (2009).
[27] J. Winkler and T. Carolus, "Trailing-edge blowing on tandem airfoils: Aerodynamic and aeroacoustic implications," AIAA Paper 2010-3981, 2010.
[28] M. Gruber, P. F. Joseph, C. Polacsek, and T. P. Chong, "Noise reduction using combined trailing edge and leading edge serrations in a tandem airfoil experiment," AIAA Paper 2012-2134, 2012.
[29] A. Manela and M. Halachmi, "Mechanisms of sound amplification and sound reduction in the flapping flight of side-by-side airfoils," J. Sound Vib. **346**, 218–228 (2015).
[30] A. Manela, "On the acoustic radiation of a pitching airfoil," Phys. Fluids **25**, 071906 (2013).
[31] S. Alben, "Optimal flexibility of a flapping appendage in an inviscid fluid," J. Fluid Mech. **614**, 355–380 (2008).
[32] S. Michelin and S. G. Llewellyn Smith, "Resonance and propulsion performance of a heaving flexible wing," Phys. Fluids **21**, 071902 (2009).
[33] S. Alben, "Passive and active bodies in vortex-street wakes," J. Fluid Mech. **642**, 95–125 (2010).
[34] P. Saffman and G. Baker, "Vortex interactions," Annu. Rev. Fluid Mech. **11**, 95–122 (1979).
[35] T. Sarpkaya, "Computational methods with vortices—The 1988 Freeman scholar lecture," J. Fluids Eng. **11**, 5–52 (1989).
[36] C. E. Brown and W. H. Michael, "Effect of leading edge separation on the lift of a delta wing," J. Aeronaut. Sci. **21**, 690–706 (1954).
[37] C. E. Brown and W. H. Michael, "On slender delta wings with leading-edge separation," NACA Technical Note No. 3430, 1955.
[38] A. Manela, "Nonlinear effects of flow unsteadiness on the acoustic radiation of a heaving airfoil," J. Sound Vib. **332**, 7076–7088 (2013).
[39] X. Dai, X. Jing, and X. Sun, "Vortex shedding and its nonlinear acoustic effect occurring at a slit," AIAA J. **49**, 2684–2694 (2011).
[40] X. Dai, X. Jing, and X. Sun, "Discrete vortex model of a Helmholtz resonator subjected to high-intensity sound and grazing flow," J. Acoust. Soc. Am. **132**, 2988–2996 (2012).
[41] M. C. A. M. Peters and A. Hirschberg, "Acoustically induced periodic vortex shedding at sharp edged open channel ends: Simple vortex models," J. Sound Vib. **161**, 281–299 (1993).
[42] M. S. Howe, "Emendation of the Brown & Michael equation, with application to sound generation by vortex motion near a half-plane," J. Fluid Mech. **329**, 89–101 (1996).
[43] M. S. Howe, *Theory of Vortex Sound* (Cambridge University Press, Cambridge, 2003).
[44] C. J. Pennycuick, "Predicting wingbeat frequency and wavelength of birds," J. Exp. Biol. **150**, 171–185 (1990).
[45] L. I. Sedov, *Two Dimensional Problems in Hydrodynamics and Aerodynamics* (Wiley, New York, 1965).
[46] S. Michelin, S. G. Llewellyn Smith, and B. J. Glover, "Vortex shedding model of a flapping flag," J. Fluid Mech. **617**, 1–10 (2008).
[47] The velocity of each vortex is also affected by its interactions with airfoils and other wake vortices (see Eq. (7) *et seq.*); yet, for the purpose of following a qualitative argument, this can be considered as a leading order estimation.
[48] A similar result was found for a single rigid airfoil conducting pitching motion, where the acoustic signal is dominated by an $O(\bar{\omega}^{5/2})$ contribution of direct motion noise at large frequencies.[30]